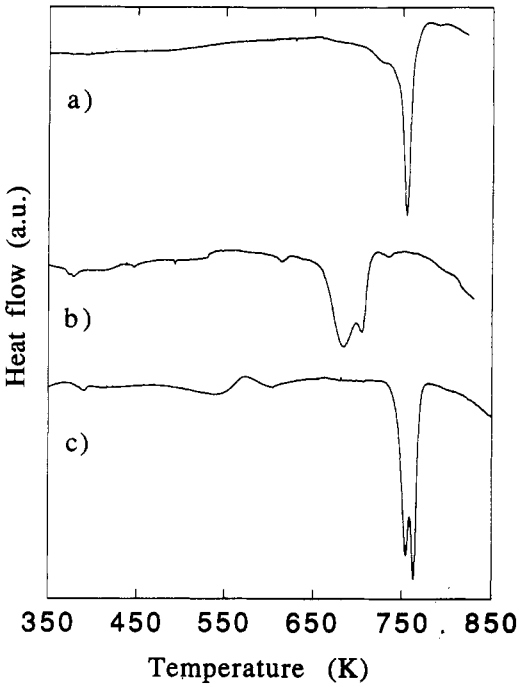

Figure 6. DSC traces of the Co–B (a), Ni–B (b), and Fe–B (c) samples.

Table III. Temperature of Crystallization T_x(onset) and Associate Enthalpy ΔH_x by DSC Data

sample	T_x (K)	ΔH_x (J/g)
Fe–B	743	176
Co–B	745	134
Ni–B	666	124

The $Q(r)$'s of all samples are very close to those of metal–boron alloys obtained by rapid quenching.[23] In particular the $Q(r)$ of Ni–B sample is very similar even in the minor details to that of a quenched sample of close composition.[24] The similarity of $Q(r)$'s in amorphous TM–B samples obtained either by chemical reduction or by rapid quenching suggests that metal–metal structuring, the dominant contribution to these curves, is similar in all samples.

All DSC traces given in Figure 6 show an exothermic signal due to sample crystallization. The onset crystallization temperature and crystallization enthalpy values, calculated from the peak areas, are given in Table III. The presence of two overlapping peaks in the Ni–B and Fe–B samples reveals a crystallization behavior which is more complex than in Co–B, which shows a sharp single peak.

XRD spectra of the powders which were treated in the DSC up to 853 K and then rapidly cooled to room temperature are shown in Figure 7. The most significant diffraction peaks in the Co–B spectrum are due to t-Co_2B,[25] and they are accompanied by faint peaks of o-Co_3B.[26] No peaks due to metallic cobalt can be identified. On the contrary, face-centered cubic (fcc) nickel[27] and α-iron peaks are present in the diffraction spectra of the Ni–B and Fe–B powders respectively. In the Ni–B sample both metal and a significant quantity of o-Ni_3B[28] are present. In the

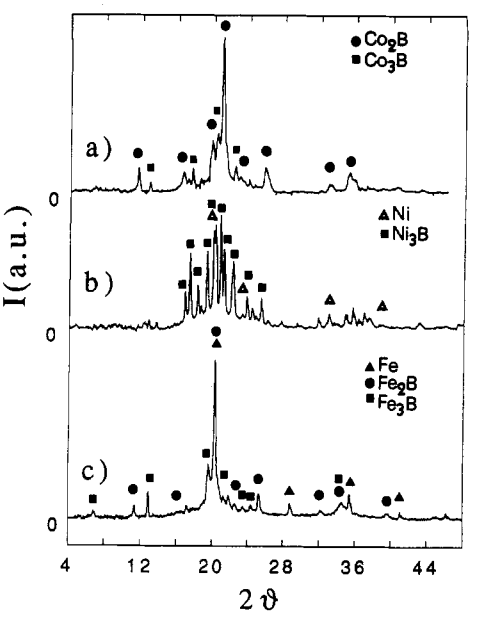

Figure 7. XRD spectra of the Co–B (a), Ni–B (b), and Fe–B (c) thermally treated samples.

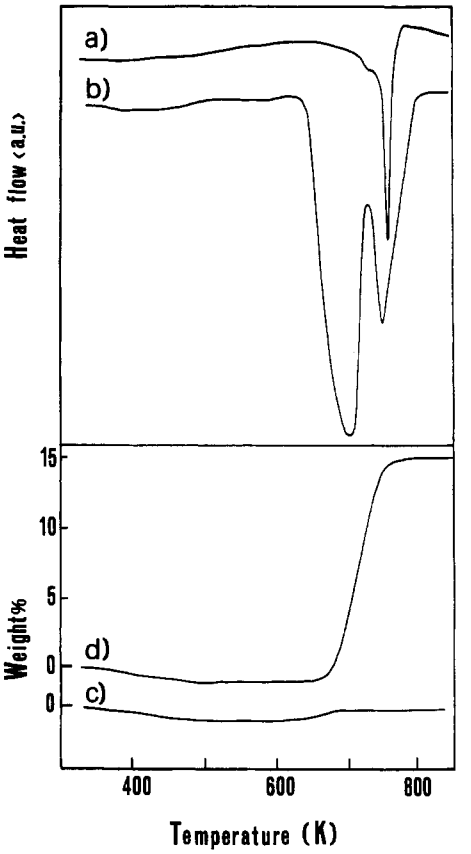

Figure 8. DSC (a, b) and TG (c, d) curves of the Co–B sample. Curves a and c refers to anaerobic condition.

Fe–B sample the dominant α-iron peaks are accompanied by those of t-Fe_2B[29] and by faint peaks arising from metastable Fe_3B.[30] These findings agree with those reported for Ni–B and Fe–B samples prepared by a similar procedure.[31,12]

To check the powders' stability at high temperatures in the presence of traces of oxygen, two different portions of

(23) Lamparter, P.; Nold, E.; Rainer-Harbach, G.; Grallath, E.; Steeb, S. Z. *Naturforsch.* **1981**, *36a*, 165.
(24) Chadha, G. S.; Cowlan, N.; Davies, H. A.; Dowald, I. V. *J. Non-Cryst. Solids* **1981**, *44*, 265.
(25) JCPDS Card No. 25-241; *Internatinal Center for Diffraction data*, 1601 Park Lane, Swartmore, PA.
(26) JCPDS Card No. 12-443.
(27) JCPDS Card No. 4-854.
(28) JCPDS Card No. 19-834.
(29) JCPDS Card No. 36-1332.
(30) JCPDS Card No. 39-1315.
(31) Carturan, G.; Enzo, S.; Ganzerla, R.; Lenarda, M.; Zanoni, R. *J. Chem. Soc., Farad. Trans.* **1990**, *86*, 739.

each sample were examined by DSC and TGA under a flow of argon containing about 10 ppm of oxygen (the same gas used for drying and passivating the powders). The DSC and TGA thermograms of the Co–B sample are reported in Figure 8. The maximum of the large exothermic DSC peak falls at the same temperature (708 K) at the inflection point in the TGA, where a weight increase of about 15% occurs. The Ni–B and Fe–B samples show a similar behavior under the same experimental conditions. Neither the DSC peak nor the TGA inflection were observed in the analogous experiments carried out under a pure (N57) argon atmosphere. The powders which result from the two experiments have a completely different appearance: those thermally treated under pure argon maintain the characteristics of the as-prepared samples, i.e., very fine, metallic-black powders, while those treated in the presence of oxygen become granular, grey, and opaque. A comparison of the XRD spectra of the two Co–B samples which underwent different thermal treatments show that the oxidized powder has a much larger fraction of fcc metallic cobalt than t-Co_2B. This is the only component present in the nonoxidized sample. In the case of the Ni–B and Fe–B samples, oxidation leads to a significant decrease of the boride phases and a corresponding increase in the metallic component. These results suggest that the TM_2B are converted to metallic particles and boron oxide through the following reaction:[7]

$$4TM_2B + 3O_2 \rightarrow 8TM + 2B_2O_3$$

As revealed by XRD, the products of all samples which form upon anaerobic crystallization have a boron content less than $TM_{60}B_{40}$. This could originate from the segregation of elemental boron which, because of its small scattering power, is not detectable by XRD. Boron could also partially form a solid solution with metals.[32] Analysis of the diffraction peak positions of both fcc nickel and α-iron shows no variations of their cell parameters.[33] This would apparently exclude the second hypothesis and suggests that excess boron segregates in an elemental form.

Acknowledgment. This work has been supported by CNR (Projet "Materiali Speciali per Tecnologie avanzate") and MURST.

(32) Ray, R.; Hasegawa, R. *Solid State Commun.* **1978**, *27*, 471.
(33) Klug, H. P., Alexander, L. E., Eds. *X-ray Diffraction Procedures for Polycrystalline and Amorphous Materials*; John Wiley & Sons: New York, 1974.

describe here the preparation of nanoscale platinum clusters of controlled dimensions which possess narrow size distributions in glassy carbon and the characterization of these materials. We also report our detailed studies of the electrocatalytic behavior of these materials and the intriguing observation that their catalytic activity is strongly coupled to the size of the platinum clusters contained in the carbon solid.

Experimental Section

All NMR spectra were obtained on Bruker AC-200, AC-250, or AC-500 spectrometers. IR spectra were recorded with a Perkin-Elmer 1600 FTIR spectrometer. XPS spectra were obtained with a Physical Electronics 550 ESCA/Auger spectrometer using a Mg anode (Mg Kα, 300 W, 15 kV). Binding energies are given relative to C(1s) at 284.6 eV. Elemental analyses were obtained from Galbraith Laboratories, Knoxville, TN, or Quantitative Technologies Inc., Whitehouse, NJ. Phenylacetylene, diisopropylamine, tetramethylethylenediamine (TMEDA), pyridine, copper(II) acetate monohydrate, copper(I) iodide, and bis(triphenylphosphine)palladium(II) chloride were used as received from Aldrich. Trimethylsilylacetylene was used as received from Farchan. Silica gel (230–420 mesh) was obtained from Brinkman. Solutions of 1 mM $K_4Fe(CN)_6$ (Mallinckrodt) were prepared in 1 M KCl in purified (Nanopure from Barnstead) water.

Poly(phenylenediacetylene). A solution of *o*-dichlorobenzene (75 mL), TMEDA (0.11 g, 0.95 mmol), copper(I) chloride (0.03 g, 0.30 mmol), and pyridine (2.5 mL) was stirred under oxygen at 65 °C. A solution of 1,3-diethynylbenzene (2.10 g, 16.7 mmol) and phenylacetylene (0.57 g, 5.6 mmol) in *o*-dichlorobenzene was added rapidly to the reaction flask. Heating and stirring under oxygen were continued for 2 h. The reaction mixture was allowed to cool to room temperature and was then stirred under oxygen for an additional 3 h. The reaction mixture was poured into acidic methanol (2% HCl) to induce precipitation and a light yellow solid was collected by centrifugation. The solid was dissolved in tetrahydrofuran (250 mL) and treated with TMEDA (0.2 mL) to remove any residual copper species in solution. This solution was then poured into acidic methanol (2% HCl) to induce precipitation and a light yellow solid (2.01 g, 75%) was collected: ^{1}H NMR (250 MHz, $CDCl_3$) δ 7.7 (s), 7.3 (s) ppm. ^{13}C NMR (62.9 MHz, $CDCl_3$) δ 136.2, 133.8, 132.8, 129.7, 128.0, 122.8, 122.6, 121.5, 81 (br), 75 (br) ppm. IR (KBr) 3050, 2200, 1578, 1463, 1377, 1084, 882, 780, 754, 679 cm^{-1}. Anal. Calcd for $C_{46}H_{22}$: C, 96.14; H, 3.86. Found: C, 96.14; H, 3.86.

Synthesis of Poly[(phenylene-1,3-diacetylene)(bis(triphenylphosphine)platinum(0))$_x$] (x = 0.2, 0.3, 0.6). To separate flasks containing 0.10 g (0.68 mmol of diyne; ~0.17 mmol of oligomer based on 4 diynes/molecule) of poly(phenylene-1,3-diacetylene) in toluene (25 mL) was added ethylene bis(triphenylphosphine)platinum(0) under argon in 0.2 (0.10 g, 0.13 mmol), 0.3 (0.15 g, 0.20 mmol), and 0.6 (0.30 g, 0.40 mmol) mol equiv relative to diyne content. The solutions were heated to 65 °C for 6 h, whereupon the solutions turned from yellow to red in color. The solutions were concentrated in vacuo to ~1/2 their original volumes and then poured into petroleum ether (250 mL). The precipitated oligomers were collected via centrifugation and washed with ethanol (3 × 100 mL) to give 50 mg (60%), 100 mg (60%), and 270 mg (69%), respectively, as light yellow powders. Poly[(phenylene 1,3-diacetylene)(bis(triphenylphosphine)platinum(0))$_x$] (x = 0.2): ^{1}H NMR (200 MHz, C_6D_6) δ 6.8 (m), 7.6 (m) ppm; ^{13}C NMR (62.9 MHz, C_6D_6) δ 136.5, 133.2, 133.0, 132.8, 129.4, 128.8, 128.6, 127.6, 122.8, 122.6, 122.5, 122.0, 83, 76 ppm; ^{31}P NMR (101.3 MHz, C_6D_6) δ 25.6 (dd, J_{P-P} = 25 Hz, J_{Pt-P} = 3440 Hz), 24.4 (dd, J_{P-P} = 25 Hz, J_{Pt-P} = 3606 Hz) ppm; ^{195}Pt NMR (64.4 MHz, C_6D_6) δ −46 74 (dd, J_{Pt-P} = 3412, 3624 Hz) ppm; IR (KBr) 3054, 2345, 2162, 1736, 1586, 1478, 1435, 1093, 792, 742, 692 cm^{-1}. Anal. Calcd for $C_{82}H_{52}P_2Pt$: C, 76.09; H, 4.05. Found: C, 75.8; H, 3.89. Poly[(phenylene 1,3-diacetylene)(bis(triphenylphosphine)platinum(0))$_x$] (x = 0.3): ^{1}H NMR (200 MHz, C_6D_6) δ 6.8 (m), 7.6 (m) ppm; ^{13}C NMR (62.9 MHz, C_6D_6) δ 136.5, 133.6, 133.0, 132.8, 129.4, 129.0, 128.6, 127.6, 122.8, 122.5, 122.0, 83, 76 ppm; ^{31}P NMR (101.3 MHz, C_6D_6) δ 25.3 (dd, J_{P-P} = 25 Hz, J_{Pt-P} = 3488); 24.8 (dd, J_{P-P} = 25 Hz, J_{Pt-P} = 3823) ppm; ^{195}Pt NMR (64.4 MHz, C_6D_6) δ −4675 (dd, J_{Pt-P} = 3665, 3579 Hz) ppm; IR (KBr) 3054, 2923, 2160, 1586, 1478, 1434, 1093, 791, 742, 693, 679 cm^{-1}. Anal. Calcd for $C_{118}H_{82}P_4Pt_2$: C, 70.37; H, 4.10. Found: C, 70.00; H, 4.18. Poly[(phenylene-1,3-diacetylene)(bis(triphenylphosphine)platinum(0))$_x$] (x = 0.6): ^{1}H NMR (200 MHz, C_6D_6) δ 6.8 (m), 7.6 (m) ppm; ^{13}C NMR (62.9 MHz, C_6D_6), δ 136.5, 133.9, 133.0, 132.8, 129.3, 128.8, 128.1, 127.6, 122.8, 122.7, 122.5, 122.0, 83, 76 ppm; ^{31}P NMR (101.3 MHz, C_6D_6) δ 25.6 (dd, J_{P-P} = 25 Hz, J_{Pt-P} = 3584), 24.7 (dd, J_{P-P} = 25 Hz, J_{Pt-P} = 3625) ppm; ^{195}Pt NMR (64.4 MHz, C_6D_6) δ −4675 (dd, J_{Pt-P} = 3656, 3543 Hz) ppm; IR (KBr) 3054, 2923, 2358, 2158, 1584, 1478, 1434, 1093, 1027, 998, 791, 742, 692 cm^{-1}. Anal. Calcd for $C_{136}H_{121}P_5Pt_{2.5}$: C, 68.12; H, 5.09. Found: C, 68.18; H, 3.97.

Poly[(2,4,5,6-tetrafluorophenylene-1,3-diacetylene)(bis(triphenylphosphine)platinum(0))$_x$]; Platinum:Diyne Ratio (x = 0.2, 0.6). To separate flasks containing 0.257 g (1.0 mmol diyne; ~0.16 mmol of oligomer based on 4 diynes/molecule) of poly(2,4,5,6-tetrafluorophenylene-1,3-diacetylene)[33] in toluene (25 mL) was added ethylene bis(triphenylphosphine)platinum(0) in 0.2 (0.14 g, 0.19 mmol) and 0.6 (0.48 g, 0.64 mmol) mol equiv relative to diyne content. The solutions were heated to 60 °C for 6 h, and the solutions turned from yellow to red in color. The solutions were concentrated in vacuo to ~1/2 their original volume and poured into petroleum ether (250 mL). The precipitated oligomers were collected via centrifugation and washed with ethanol (3 × 100 mL) to give (0.30 g, 80%) and (0.20 g, 75%), respectively, as light yellow powders. Poly[(2,4,5,6-tetrafluorophenylene-1,3-diacetylene)(bis(triphenylphosphine)platinum(0))$_x$]; (x = 0.2): ^{1}H NMR (200 MHz, C_6D_6) δ 7.13 (m), 7.39 (m) ppm; ^{13}C NMR (62.9 MHz, C_7D_8) δ 167.2, 155.0, 150.1, 137.7, 133.0, 132.6, 128.2, 127.6, 126.5, 97.1, 83.2, 68.0, ppm; ^{31}P NMR (101.3 MHz, C_6D_6) δ 24.5 (m, J_{Pt-P} = 3565 Hz), 22.4 (m, J_{Pt-P} = 3823 Hz) ppm; ^{195}Pt NMR (64.4 MHz, C_6D_6) δ −4594 (dd, J_{Pt-P} = 3705, 3550 Hz) ppm; IR (KBr) 3090, 3070, 3035, 2189, 2173, 1620, 1479, 1436, 1390, 1079, 1035, 963, 744, 674 cm^{-1}. Anal. Calcd for $C_{112}H_{30}F_{34}P_2Pt$: C, 59.04; H, 1.33. Found: C, 58.39; H, 1.84. Poly[(2,4,5,6-tetrafluorophenylene 1,3-diacetylene)(bis(triphenylphosphine)platinum(0))$_x$] (x = 0.6): ^{1}H NMR (200 MHz, C_6D_6) δ 7.15 (m), 7.42 (m) ppm; ^{13}C NMR (62.9 MHz, C_7D_8) δ 167.3, 154.8, 149.7, 136.2, 134.0, 133.0, 118.6, 84.0, 68.5 ppm; ^{31}P NMR (101.3 MHz, C_6D_6) δ 24.5 (m, J_{Pt-P} = 3610 Hz), 22.5 (m, J_{Pt-P} = 3810 Hz) ppm; ^{195}Pt NMR (64.4 MHz, C_6D_6) δ −4593 (dd, J_{Pt-P} = 3715, 3610 Hz) ppm; IR (KBr) 3090, 3070, 3035, 2188, 1960, 1815, 1619, 1478, 1436, 1390, 1097, 1035, 963, 744, 674 cm^{-1}. Anal. Calcd for $C_{220}H_{120}F_{34}P_8Pt_4$: C, 59.55; H, 1.33. Found: C, 60.06; H, 1.26.

Preparation of Pt-GC6 and Pt/F-GC6 Films on Conventional Glassy Carbon. Glassy carbon disks (1.5-cm diameter, Atomergic GC25) were washed with acetone and distilled water and then sonicated in distilled water for 5 min. The disks were dried in a vacuum oven (65 °C, 0.15 mmHg) and then affixed to a Headway Research Inc. Model PWM101-PMR485 photoresist spinner. Separate saturated solutions of the oligomers above in toluene (5 mL) were added dropwise to the glassy carbon disk (rotating at a rate of 200 rpm) until the disk was completely covered with the solution. Spinning was continued at a constant rate until evaporation of the toluene was complete (~5 min). This procedure provided reproducible, homogeneous films with thicknesses in the range 1–5 μm. The thin films on glassy carbon were placed in a quartz tube which was inserted into a furnace such that one portion of the tube extended outside the furnace for connection to an oil diffusion vacuum pump. The vessel was evacuated (10^{-3} to 10^{-6} mmHg) and then heated at a rate of 1 °C/min to 600 °C. Thermal treatment at 600 °C was continued for 6 h. The samples were then cooled to room temperature at a rate of ~10 °C/min and then removed from the tube as a dark, highly reflective films on the glassy carbon substrate. Thermolysis of poly[(phenylene-1,3-diacetylene)(bis(triphenylphosphine)platinum(0))$_x$] (x = 0.2, 0.3, 0.6) gave 0.90, 1.1, and 1.5 Pt atom % **Pt-GC6**, respectively, and thermolysis of poly[(2,4,5,6-tetrafluorophenylene-1,3-diacetylene)(bis(triphenylphosphine)-

(33) Hutton, H. D.; Huang, W.; Alsmeyer, D. C.; Kometani, J.; McCreery, R. L.; Neenan, T. X.; Callstrom, M. R. *Chem. Mater.* **1993**, *5*, 1110.

platnum(0))$_x$]; platinum:diyne ratio (x = 0.2, 0.6) gave 0.50 and 1.5 Pt atom % **Pt/F-GC6**, respectively.

Preparation of PtO_2/GC6. In separate flasks containing 0.13 g (~0.23 mmol oligomer based on 4 diynes/molecule) of finely powdered poly(phenylene-1,3-diacetylene) was added 5 wt % (7 mg, 0.03 mmol) and 20 wt % (27 mg, 0.12 mmol) of platinum(IV) oxide, and the contents were mixed in a Wig-L-Bug for 60 s. The powdered oligomer/platinum oxide mixtures were separately added to 1-cm diameter circular die and pressure (6800 bars) was applied. For each sample, the die was heated to 330 °C for 1 h (heating rate 20 °C/min) and then allowed to cool slowly to room temperature. The dark disks produced were placed in a quartz tube and heated to 600 °C (rate 1 °C/min) under dynamic vacuum (0.005 Torr) and held at 600 °C for 6 h. After cooling to room temperature, the 0.25 and 1 Pt atom % **PtO_2/GC6** disks were removed from the quartz tube.

Electrochemical Reduction of Platinum Oxide Doped Glassy Carbon. A **PtO_2/GC6** disk containing a 1 atom % Pt was subjected to a reducing potential (−1 V vs SCE) in a 0.5 M sulfuric acid solution for 10 min. The disk was removed from the solution and rinsed with deionized water.

Electron Microscopy Studies. For scanning electron microscopy (SEM) studies, uncoated thin-film specimens of X-GC6 materials on GC and gold-coated disks of **PtO_2/GC6** were examined on a Hitachi Model S-510 instrument operated at 25 keV. For transmission electron microscopy (TEM), electron-transparent films were prepared on potassium bromide disks. Following dissolution of the salt in deionized water, the X-GC6 films were picked up on 1000 mesh Cu support grids. Upon drying, the samples were examined on a Zeiss EM902 electron microscope, operated at 80 keV equipped with an energy-loss imaging system. The resolution of the EM902 instrument is approximately 4 Å in bright-field mode. Virtually achromatic bright-field images were obtained at an energy loss (ΔE) of 0 eV by inserting a 30-eV energy slit into the energy-dispersed electron energy-loss spectrum, which permitted acquisition of unscattered and elastically-scattered electrons for image formation without image-degrading inelastically scattered electrons. This protocol yields contrast-enhanced images.[34] High-resolution TEM images were obtained on a Hitachi H9000 NAR electron microscope operated at 300 keV near the optimal Scherzer defocus with a resolution of approximately 1.8 Å.

General Procedure for Voltammetry. Cyclic voltammetry was performed with a triangle wave generator and personal computer as described elsewhere.[35] The active electrode area was determined by a Teflon washer and measured approximately 0.01–0.1 cm^2, with each electrode area determined by chronoamperometry of $Fe(CN)_6^{3-/4-}$. Voltammery on the **Pt/F-GC6** electrodes was performed immediately after removal from the vacuum curing apparatus. For other thin-film electrodes, electrodes were pretreated for 1 h a 500 °C in an argon atmosphere, immediately before voltammetry experiments. Solutions were degassed with argon before use, and an argon stream was maintained over the solution during voltammetric measurements. Voltammetry of the hydrogen evolution reaction (HER) was carried out in 1 M $HClO_4$ immediately after electrode preparation. The **Pt-GC6** surface was pretreated by 10 potential scans (200 mV/s) between +1.0 and −0.20 V vs SSCE followed by a potential step to −0.8 V for 30 s, and a final scan between +1.2 and 0 V. The oxygen reduction reaction (ORR) was studied using the same procedure in O_2-saturated 1 M $HClO_4$. Following pretreatment, a voltammogram was obtained at 50 mV/s, which was fast enough to avoid significant gas evolution. For a given **Pt-GC6** electrode, the potential cycling pretreatment was repeated after any changes in the electrolyte. Geometric (i.e., projected) electrode areas were determined by chronoamperometry of $Fe(CN)_6^{4-}$ in 1 M KCl, after completion of experiments on electrocatalysis. In all cases, the reference electrode was a sodium-saturated calomel electrode (SSCE, +0.236 V vs NHE).

(34) For a complete description on the operation of the EM902, see: Samseth, J.; Mortensen, K.; Burns, J. L.; Spontak, R. J. *J. Appl. Polym. Sci.* **1992**, *44*, 1245.

(35) Allred, C. D.; McCreery, R. L. *Anal. Chem.* **1992**, *64*, 444.

Scheme II

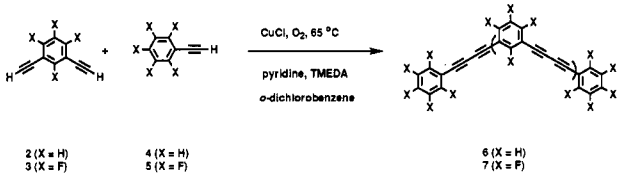

Scheme III

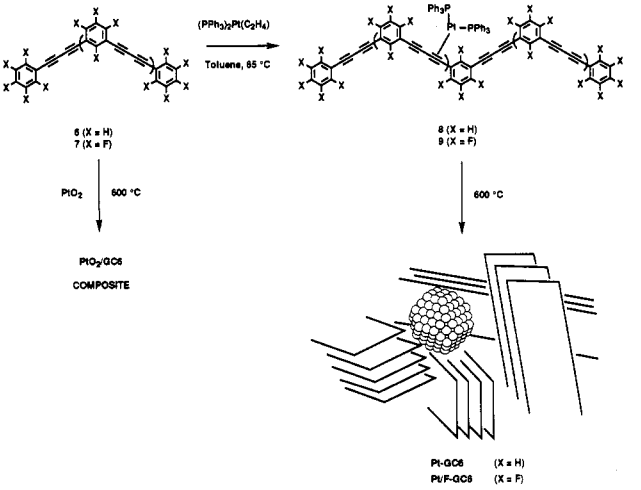

Results and Discussion

1. Synthesis. Preparation of the glassy carbon solids begins with the oligomerization of the highly unsaturated diethynylbenzene derivatives, 1,3-diethynylbenzene (**2**) and 1,3-diethynyl-2,4,5,6-tetrafluorobenzene (**3**). We utilized the Glaser oxidative coupling of **2** or **3**, using copper chloride as a catalyst in *o*-dichlorobenzene, to form poly(phenylene-1,3-diacetylene) (**6**) or poly(2,4,5,6-tetrafluorophenylene-1,3-diacetylene) (**7**) (Scheme II).[36] To maintain solubility, approximately 30 mol % of phenyl acetylene (**4**) or pentafluorophenyl acetylene (**5**) was added to the reaction solutions to serve as end-capping groups and to limit the molecular weight of the oligomers formed. In general, the oligomers formed with these ratios of diacetylene:monoacetylene yields materials with good solubility and film-forming behavior.

To derive new catalytic activity with glassy carbon solids derived from these precursors, we explored the incorporation of metals into the carbon matrix. Our initial experiments relied on a simple strategy: the admixing of microcrystalline platinum oxide with **6** to generate a **PtO_2/GC6** composite (Scheme III). The resultant material, characterized below, consists of 1–20-μm-diameter microcrystallites of PtO_2 immobilized within a glassy carbon matrix. These materials exhibited good electrocatalytic activity for the generation of dihydrogen from an acidic solution;[30] however, the utilization of the platinum contained in the electrode was far from optimal because of the relatively low surface-to-volume ratio of the microcrystallites.

From these results we recognized that the preparation of much more highly dispersed metal clusters in glassy carbon was likely to result in higher catalytic activity.[37] However, a greater level of dispersion of a metal catalyst on a support is not the only factor to consider in the design of new catalytic surfaces. It is widely recognized that the

(36) Hay, A. S. *J. Org. Chem.* **1960**, *25*, 1275.

(37) Davis, S. C.; Klabunde, D. J. *Chem. Rev.* **1982**, *82*, 153.

catalytic activity and selectivity of metals supported on various surfaces is controlled by several important factors, including (1) the size, shape, and composition of the metal catalyst, (2) the composition of the support, (3) the surface functionality of the support, and (4) the physical and electronic interaction of the support and the metal catalyst.[38] In particular, effecting control of these factors is critically important for the use of supported metal catalysts in fuel-cell applications.[39-45]

In an attempt to address these important factors, platinum was incorporated into the glassy carbon precursors by coordination of a platinum complex to the carbon–carbon triple bond of **6** or **7** in Scheme III. Reaction of **6** with ethylene bis(triphenylphosphine)-platinum(0) in 0.2–0.6 mol equiv of the platinum complex relative to the diacetylene functionality contained in **6**, in toluene at 25 °C under an argon atmosphere for 6 h, resulted in the formation of poly[(phenylene-1,3-diacetylene)(bis(triphenylphosphine)platinum(0))$_x$] (x = 0.2, 0.3, 0.6) (**8**).[46,47] Addition of the reaction solution to an excess of petroleum ether resulted in the precipitation of **8** as a green-yellow solid in 69% yield. This solid was air-stable and soluble in toluene and benzene. Prolonged reaction (3 days) under the same conditions resulted in the formation of an intractable solid, presumably resulting from displacement of triphenylphosphine ligands from platinum by alkynes on other polymer chains. The fluorine-containing GC precursor, poly[(2,4,5,6-tetrafluorophenylene-1,3-diacetylene)(bis(triphenylphosphine)-platinum(0))$_x$ (x = 0.2, 0.6; **9**), was prepared in an analogous fashion from **7** as described above.

We chose to prepare these particular GC precursors for three primary reasons: (1) this method of preparing **8** and **9** allows the atomic dispersion of platinum along the diacetylenic polymer backbone, (2) we anticipated that the triphenylphosphine ligands of **8** and **9** would be readily lost on thermolysis, and (3) the incorporation of high levels of fluorine in the carbon solid in **9** might enhance the adsorption of dioxygen to the electrode surface and assist its catalytic reduction.

The platinum-containing GC precursors (**8** and **9**) were characterized by a combination of ^{31}P and ^{195}Pt NMR spectroscopies in addition to the usual spectroscopic and analytical methods. Figure 2A shows the ^{31}P NMR spectrum obtained on examination of (1,4-diphenylbutadiyne)bis(triphenylphosphine)platinum(0) (**10**) in

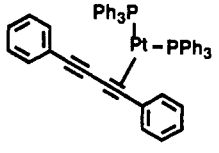

10

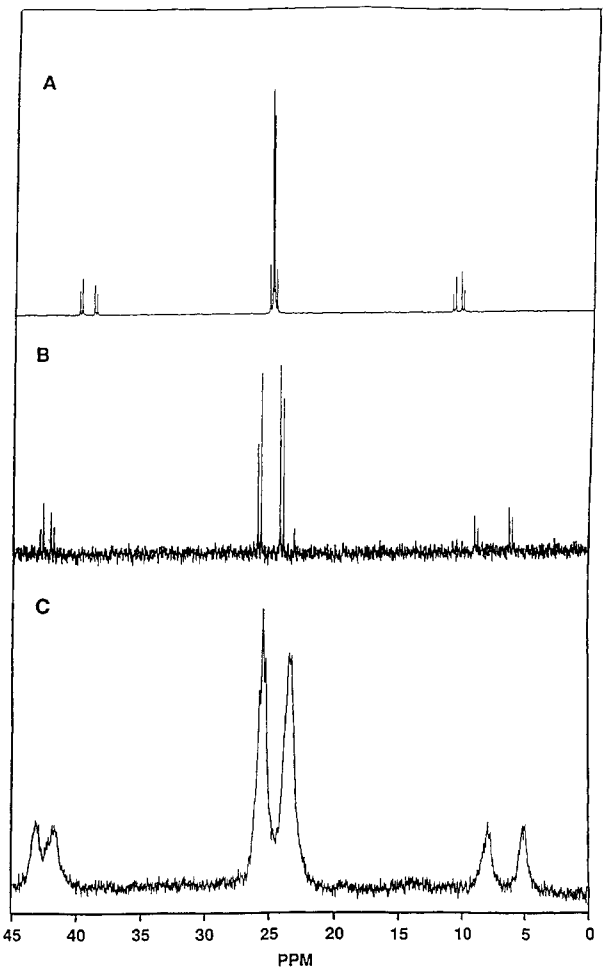

Figure 2. ^{31}P NMR spectra of (A) (1,4-diphenylbutadiyne)bis-(triphenylphosphine)platinum(0) (**10**), (B) poly[(phenylene-1,3-diacetylene)(bis(triphenylphosphine)platinum(0))$_{0.2}$] (**8**), and (C) poly[(2,4,5,6-tetrafluorophenylene-1,3-diacetylene)(bis(triphenylphosphine)platinum(0))$_{0.2}$] (**9**).

benzene-d_6 at 121.5 MHz.[48] This spectrum illustrates that the two phosphorus atoms in **10** are not equivalent, giving the expected AB quartet coupling pattern with chemical shifts of 25.37 and 25.62 ppm (J_{P-P} = 25 Hz). The ^{31}P nuclei are also coupled to ^{195}Pt (natural abundance of 33.8%) with coupling constants of 3373 and 3598 Hz. Figure 2B shows the ^{31}P NMR spectrum of **8** in which the diyne: platinum ratio was 1:0.2. The spectrum is similar to that found for **10** with an AB quartet for the inequivalent phosphorus nuclei. Importantly, the chemical shifts of 25.6 and 24.4 ppm (J_{P-P} = 25 Hz) and Pt–P coupling constants of 3440 and 3606 Hz are quite similar to that found for **10**, indicating that the assigned structure for **8** is correct. The ^{31}P NMR spectrum of **9**, in which the diyne: platinum ratio was also 1:0.2, is qualitatively similar to that found for **8** and **10** (Figure 2C). However, coupling between ^{31}P and ^{19}F significantly broadens the ^{31}P NMR spectrum.

These same complexes were examined by ^{195}Pt NMR (Figure 3). Figure 3A shows the ^{195}Pt NMR spectrum obtained on examination of **10**. A ^{195}Pt chemical shift of −4704 ppm with Pt–P coupling constants of 3405 and 3614 Hz was observed. Figure 3B shows the ^{195}Pt NMR spectrum of **8** which is quite similar to that of the model compound **10** with a ^{195}Pt chemical shift of −4674 ppm

(38) *Metal Clusters in Catalysis*; Gates, B. C., Guczi, L., Knözinger, H., Ed.; Elsevier: New York, 1986.
(39) Blurton, K. F.; Greenberg, P.; Oswin, H. G.; Rutt, D. R. *J. Electrochem. Soc.* **1972**, *119*, 559.
(40) Bregoli, L. J. *Electrochim. Acta* **1978**, *23*, 489.
(41) Peuckert, M.; Yoneda, T.; Dalla Betta, R. A.; Boudart, M. *J. Electrochem. Soc.* **1986**, *133*, 944.
(42) Sattler, K.; Ross, P. N. *Ultramicroscopy* **1986**, *20*, 21.
(43) Watanabe, M.; Saegusa, S.; Stonehart, P. *Chem. Lett.* **1988**, 1487.
(44) Kinoshita, K. *J. Electrochem. Soc.* **1990**, *137*, 845.
(45) Srinivasan, S. *J. Electroanal. Chem.* **1981**, *118*, 51.
(46) Hartley, F. R. *Complexes of Zerovalent Platinum and Palladium*; Applied Science Publishers Ltd.: London, 1973; p 398.
(47) Blake, D. M.; Roundhill, D. M. *Inorg. Synth.* **1979**, *19*, 120.
(48) Heyns, J. B.; Stone, F. G. A. *J. Organomet. Chem.* **1978**, *160*, 337.

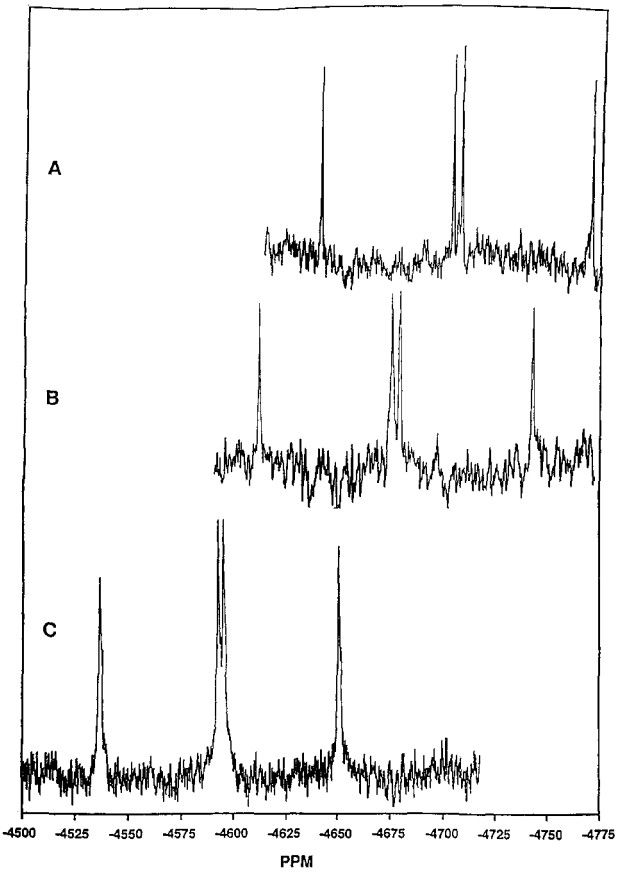

Figure 3. ^{195}Pt NMR spectra of (A) (1,4-diphenylbutadiyne)-bis(triphenylphosphine)platinum(0) (**10**), (B) poly[(phenylene-1,3-diacetylene)(bis(triphenylphosphine)platinum(0))$_{0.2}$] (**8**), and (C) poly[(2,4,5,6-tetrafluorophenylene-1,3-diacetylene)(bis(triphenylphosphine)platinum(0))$_{0.2}$] (**9**).

and Pt–P coupling constants of 3412 and 3624 Hz. The ^{195}Pt NMR spectrum of the fluorinated GC precursor, **9**, is also qualitatively similar to that of **10** (Figure 3C). As might have been expected for the perfluorinated analog of **8**, the ^{195}Pt chemical shift of **9** is further downfield at −4594 ppm. The Pt–P coupling constants for **9** are of the same magnitude as those observed for **8** and **10** with values of 3550 and 3703 Hz. The small differences in the ^{195}Pt and ^{31}P NMR chemical shifts for **8** and **9** relative to those found for the model compound **10**, in addition to the similar Pt–P coupling constants, provide convincing evidence that the platinum is present in the oligomer as depicted, and that no other forms of platinum are present in the GC precursor.

Conversion of **8** and **9** to a material composed of nanoscale platinum clusters in glassy carbon (**Pt-GC6**) or in fluorine-doped glassy carbon (**Pt/F-GC6**) was accomplished by casting a thin film of **8** or **9**, dissolved in toluene, onto a conventional glassy carbon disk or onto a potassium bromide disk, followed by thermolysis at 600 °C (1 °C/min ramp rate, 6 h at final temperature) at 10^{-6} Torr (Scheme III). The **Pt-GC6** and **Pt/F-GC6** materials produced were black, highly reflective, and conductive (the idealized structure shown in Scheme III is explained below).

2. Characterization of Platinum-Doped GC Materials. We compare here GC containing platinum oxide dispersed in the carbon matrix and GC containing nanoscale platinum clusters. The surface composition and the oxidation state of the platinum contained in the carbon

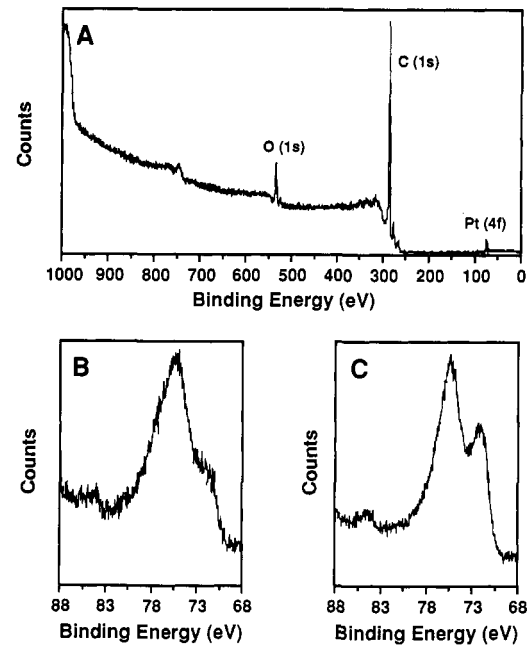

Figure 4. X-ray photoelectron spectra of **PtO_2/GC6**: (A) survey analysis of **PtO_2/GC6**; (B) high-resolution spectrum of the Pt-(4f) region of **PtO_2/GC6**; (C) high-resolution spectrum of the Pt(4f) region of **PtO_2/GC6** following exposure of the sample to a reducing potential (−1 V vs SCE) in 0. 5 M sulfuric acid for 10 min.

matrices of these materials have been investigated by X-ray photoelectron spectroscopy (XPS). The morphologies of films and solid disks of these materials have been examined by scanning electron microscopy (SEM) and transmission electron microscopy (TEM) has been used to characterize the nanoscale platinum particles in the X-GC6 platinum-doped materials.

X-ray Photoelectron Spectroscopy. Figure 4 contains the XPS spectra of **PtO_2/GC6**. The survey spectrum of this sample clearly shows the presence of oxygen [O(1s) at ~535 eV], carbon [C(1s) at ~290 eV] and platinum [Pt(4f) at ~75 eV] (Figure 4A). As seen in the high-resolution spectrum of the Pt(4f) electron region of the **PtO_2/GC6** material, the platinum in the material is a mixture of Pt(0), Pt(II), and Pt(IV) oxidation states (Figure 4B). Application of a reducing potential of −1 V vs SCE in 0.5 M sulfuric acid resulted in substantial reduction of a portion of the oxidized platinum to Pt(0). This reduction is evidenced by the growth of the Pt($4f_{7/2}$) line at approximately 72 eV as seen on comparison of the Pt(4f) electron region before reduction (Figure 4B) and after reduction (Figure 4C).

The XPS spectra of **Pt-GC6** and **Pt/F-GC6** are provided in Figure 5. Figure 5A,C clearly shows that these materials possess only a residual level of oxygen and that fluorine is retained in the **Pt/F-GC6** solid at a level of approximately 15 atom %. Of particular concern is the fate of the triphenylphosphine on thermal treatment of **8** and **9** (Scheme III). Careful examination of the spectra presented in Figure 5A,C found that >95% of the phosphorus is lost on thermal treatment, resulting in a residual level (<0.1 atom %) of phosphorus in the solid.[49] Comparison of the areas of the Pt(4f) and C(1s) regions for each of the materials prepared found that platinum is present in these

(49) The P(2p) electrons is found at approximately 132 eV. The expressed residual level is an estimate of the detection limit of the spectrometer for phosphorus.

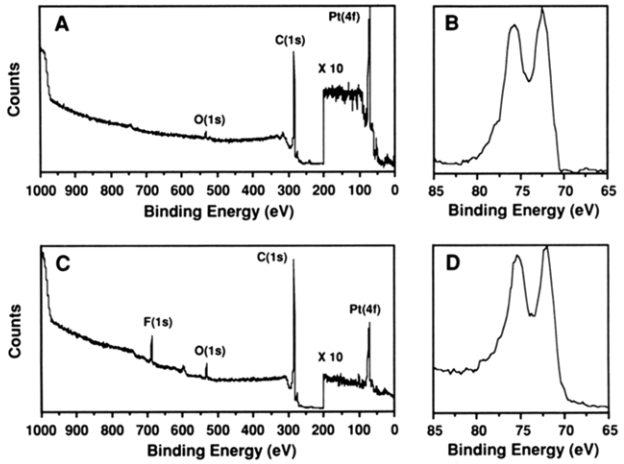

Figure 5. (A) XPS survey spectrum of 0.9 Pt atom % **Pt-GC6** following an argon ion sputter treatment. (B) High-resolution spectrum of the Pt(4f) line in **Pt-GC6**. (C) XPS survey spectrum of 0.5 Pt atom % **Pt/F-GC6** following an argon ion sputter treatment. (D) High-resolution spectrum of the Pt(4f) line in **Pt/F-GC6**.

materials ranging from 0.50 to 1.5 Pt atom % with the ultimate loading of platinum in the solid proportional to the platinum content in the GC precursors. Thermolysis of poly[(phenylene-1,3-diacetylene)(bis(triphenylphosphine)platinum(0))$_x$ (**8**) with x = 0.2, 0.3, and 0.6 gave **Pt-GC6** containing 0.90, 1.1, and 1.5 Pt atom %, respectively. Similarly, poly[(2,4,5,6-tetrafluorophenylene-1,3-diacetylene)(bis(triphenylphosphine)platinum(0)$_x$] with x = 0.2 and 0.6 gave **Pt/F-GC6** containing 0.50 and 1.5 Pt atom %, respectively.

High-resolution spectra of the Pt(4f) electron region of **Pt-GC6** and **Pt/F-GC6** are presented in Figure 5B,D, respectively. Examination of these spectra found predominately a single oxidation state for the platinum with the expected Pt($4f_{7/2}$/$4f_{5/2}$) doublet. The binding energy of the C(1s) electron from each analysis was used as an internal reference (284.6 eV) for determination of the binding energies of the Pt($4f_{7/2}$) electrons which produced values of 72.3 and 71.9 eV, respectively. These values are approximately 1 eV higher in binding energy than that found for bulk polycrystalline platinum. While the higher binding energies observed for the Pt(4f) electrons in these specimens are not attributed to the presence of oxidized platinum as evidenced by previous electron diffraction studies,[32] the higher binding energies may be due to the effect of small particles on binding energy and/or because of the intimate interaction of the platinum particles with the conductive carbon substrate.[50-53] These XPS data clearly demonstrate that thermolysis of poly(phenylene-diacetylene) materials containing bis(triphenylphosphine)-platinum dispersed along the oligomeric backbone provides for the formation of Pt(0) in the carbon matrix with the loss of phosphorus from the material.

Electron Microscopy. Examination of **PtO_2/GC6** by scanning electron microscopy found, as expected, PtO_2 particles evenly dispersed in GC (Figure 6). These particles, the light features evident in Figure 6, are

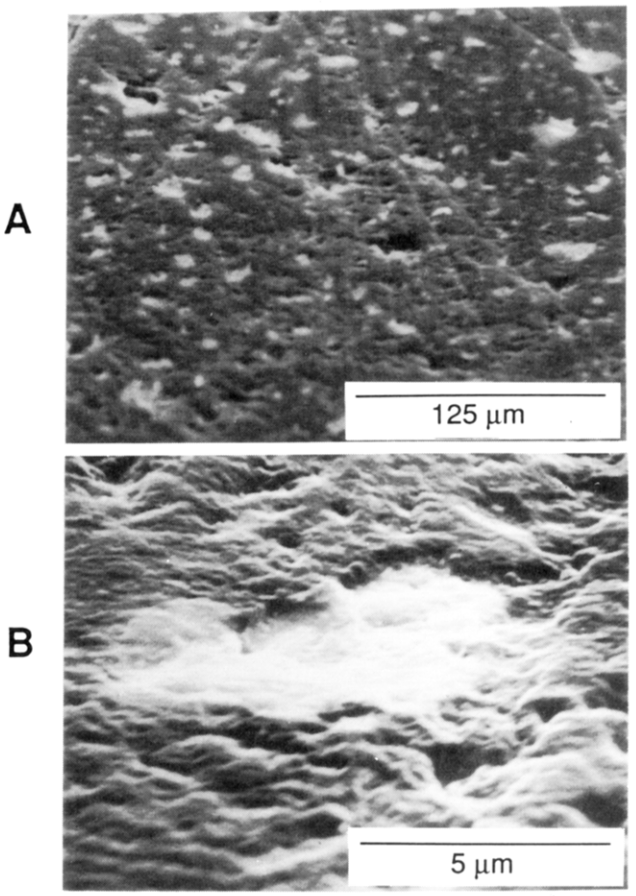

Figure 6. Scanning electron micrographs of gold-coated **PtO_2/GC6**: (A) the surface at low magnification and (B) the same region at higher magnification showing a single particle. The light features are PtO_2, and the dark background is GC.

relatively large with approximate diameters from 1–20 μm. In sharp contrast to these materials, films composed of **Pt-GC6** or **Pt/F-GC6** on conventional GC, prepared by spin-coating dilute toluene solutions of **8** or **9** onto GC followed by thermal treatment at 600 °C and 10^{-6} Torr, are completely homogeneous at these magnification levels (Figure 7). The resultant films measure approximately 2 μm thick and appear smooth and free from macroscopic cracks removed from the edge of the film (Figure 7B). Micrographs of the interior of the films are featureless. The micrographs in Figure 7 were taken at the edge of the film where fracture occurred to show the thickness of the film. This fracture edge was presumably formed by the buildup of material near the edge of the disk which then cracked due to thermal stress. Films of these **X-GC6** materials for catalysis studies are routinely prepared on a variety of surfaces including high surface area carbons.

Transmission electron microscopic analyses of **Pt-GC6** and **Pt/F-GC6** were carried out to determine the size, distribution, and state of the platinum clusters contained in the carbon matrix.[32] The series of micrographs presented in Figure 8 correspond to doping levels of 0.90 Pt atom % (Figure 8A), 1.1 Pt atom % (Figure 8B), and 1.5 Pt atom % (Figure 8C). Image analysis of each of the micrographs in Figure 8A–C yielded the cluster-size histograms also shown. The clusters in the 0.9 Pt atom % **Pt-GC6** material were found to have an average diameter of 8 Å, with clusters ranging in size from the resolution limit of the microscope (4 Å point-to-point) to 14 Å. Similarly, the 1.1 Pt atom % **Pt-GC6** specimen consists of clusters with an average diameter of 10 Å, with

(50) Eberhardt, W.; Fayet, P.; Cox, D.; Fu, Z.; Kaldor, A.; Sherwood, R.; Sondericker, D. *Phys. Rev. Lett.* **1990**, *64*, 780.
(51) Eberhard, W.; Fayet, P.; Cox, D.; Fu, Z.; Kaldor, A.; Sherwood, R.; Sondericker, D. *Phys. Scr.* **1990**, *41*, 892.
(52) Kim, K. S.; Winograd, N. *Chem. Phys. Lett.* **1975**, *30*, 91.
(53) Takasu, Y.; Unwin, R.; Tesche, B.; Bradshaw, A. M.; Grunze, M. *Surf. Sci.* **1978**, *77*, 219.

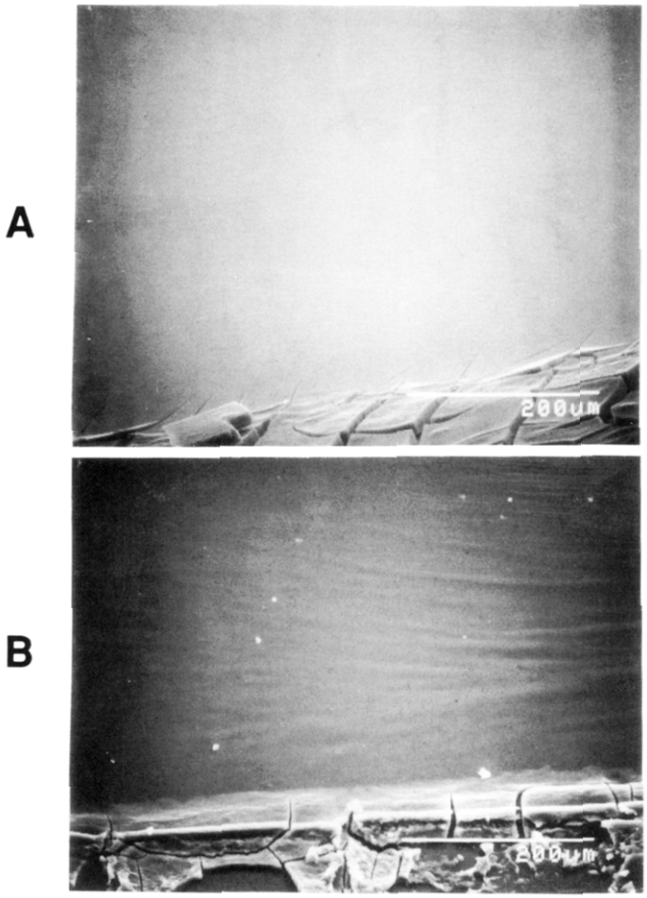

Figure 7. (A) Scanning electron micrograph of a thin film of 0.90 Pt atom % **Pt-GC6** on a conventional glassy carbon disk; and (B) scanning electron micrograph of 0.50 Pt atom % **Pt/F-GC6** on a conventional glassy carbon disk. In each micrograph, the films are cracked in the lower portion of the micrographs and the continuous **X-GC6** film covers the remainder of the disk.

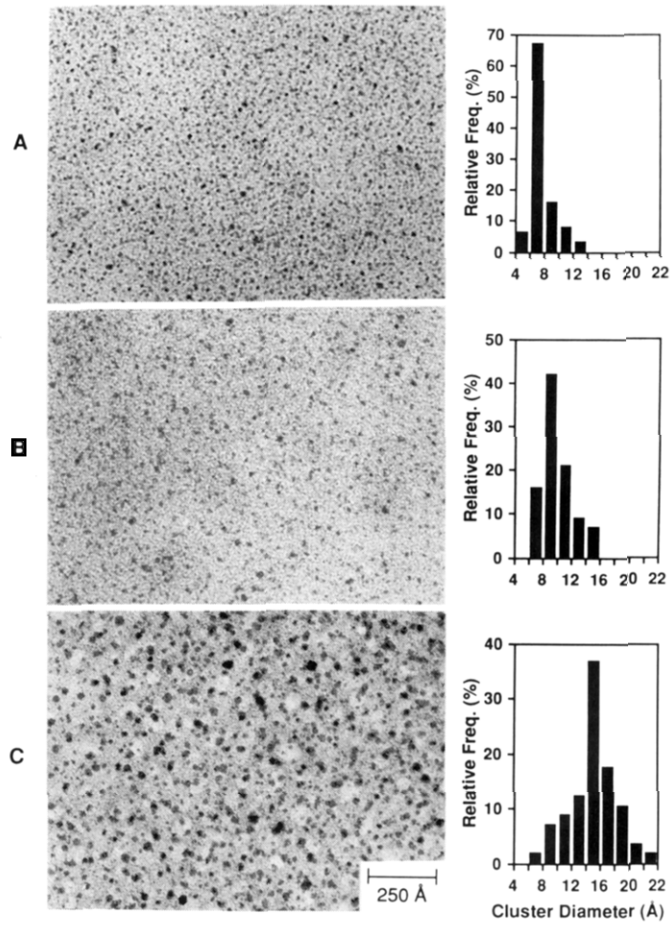

Figure 8. Bright-field images and corresponding cluster size distribution of **Pt-GC6** at different platinum loadings. (A) 0.90 Pt atom %, average cluster size = 8 Å. (B) 1.1 Pt atom %, average cluster size = 10 Å. (C) 1.5 Pt atom %, average cluster size = 15 Å.

clusters from 6 to 16 Å in diameter. The clusters in the 1.5 Pt atom % **Pt-GC6** material possess an average diameter of 15 Å and range in size from 6 to 22 Å. A greater concentration of platinum contained in 8 clearly leads to larger platinum clusters. For the 0.9 Pt atom % sample, clusters with diameters from 6 to 8 Å constitute over 65% of the clusters present in the material and the range of clusters present is only 10 Å. Similarly for the 1.1 Pt atom % sample, the range of cluster diameters is only 10 Å with the majority of the clusters between 8 and 12 Å in diameter. The most concentrated sample contains clusters significantly larger than the other two samples, dominated by clusters with diameters between 14 and 16 Å, and the range of clusters diameters is somewhat greater (16 Å). We anticipate that optimization of the experimental parameters related to the formation of the platinum clusters would generate materials possessing even narrower size distributions.

High-resolution TEM images of 0.5 and 1.5 Pt atom % **Pt/F-GC6** obtained near the optimum Scherzer defocus are shown in Figure 9A,B, respectively. The dark striated dispersions in these micrographs correspond to platinum clusters, whereas the lighter disordered features arise from graphitic carbon which constitutes the glassy carbon support. The platinum clusters present in the 0.5 Pt atom % **Pt/F-GC6** sample possess an average diameter of 14 Å, while the 1.5 Pt atom % sample platinum clusters possess an average diameter of 19 Å. These clusters are similar in size to the analogous **Pt-GC6** series discussed above. Analogous to our previously reported study of a **Pt-GC6** specimen consisting of 32-Å average diameter platinum clusters,[32] close examination of the higher magnification micrographs of Figure 9A,B reveals that many of the platinum clusters in **Pt/F-GC6** exhibit lattice fringes, indicative of crystalline order.

The structure shown for **Pt-GC6** and **Pt/F-GC6** in Scheme III represents that the carbon matrix in these solids is similar to conventionally prepared glassy carbon which is illustrated by the small domains of graphitic ribbon. The scheme also shows one platinum cluster with a defect-free cubooctahedral structure containing 201 atoms. This cluster possesses a diameter of approximately 18 Å, which lies close to the average nanocluster size obtained by TEM analysis for these materials.[42,54,55] Undoubtedly, the platinum clusters contained in these solids are not defect-free, a feature which may have a significant impact on the catalysis mediated by these materials which is described below. Remarkable features of our methodology which are apparent from these structural studies included (1) the platinum clusters present in these materials are homogeneous throughout the carbon matrix, (2) the platinum clusters possess a relatively narrow size distribution, (3) the platinum concentration effectively controls the size of clusters that

(54) van Hardeveld, R.; Hartog, F. *Surf. Sci.* **1969**, *15*, 189.
(55) Wang, S.-W.; Falicov, L. M.; Searcy, A. W. *Surf. Sci.* **1984**, *143*, 609.

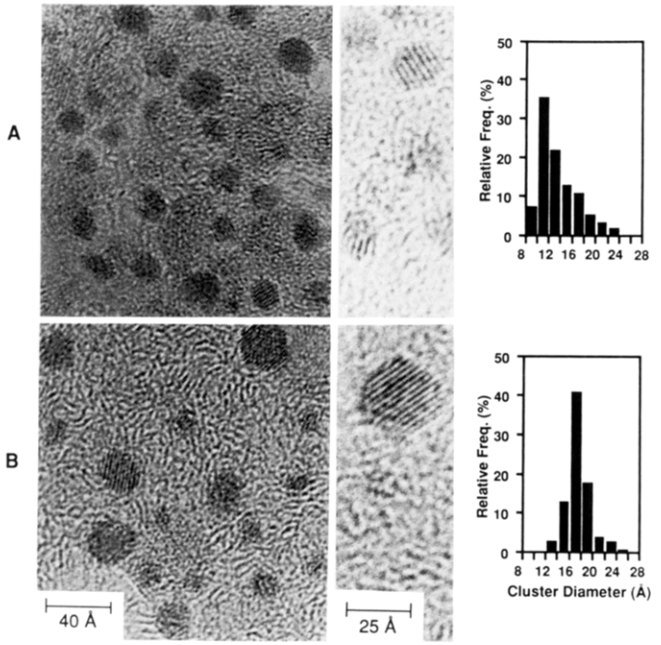

Figure 9. Bright-yield TEM micrographs obtained near the optimum Scherzer defocus of representative areas of **Pt/F-GC6** containing: (A) 0.5 atom % platinum revealing the lattice fringes of the platinum particles. The average particle diameter is 14 Å, with the cluster size distribution shown at the right. (B) 1.5 atom % platinum revealing the lattice fringes of the platinum particles. The average particles diameter is 19 Å, with the cluster size distribution shown at the right.

are generated in the carbon matrix, and (4) the platinum clusters are crystalline.

3. Electrochemistry of Pt-GC6 and Pt/F-GC6. Examination of the **Pt-GC6** materials for electrocatalytic performance will be discussed in the next three sections. First, a semiquantitative comparison of various **Pt-GC6** and **Pt/F-GC6** materials for hydrogen evolution and dioxygen reduction will be presented. Second, the quantitative issues of microscopic surface area and particle accessibility will be considered. Third, the mechanistic implications of the results are discussed, with particular attention to differences between nanoscale Pt(0) cluster behavior and that of bulk polycrystalline Pt.

Voltammograms for several related electrode materials in 1 M $HClO_4$ are shown in Figure 10. Curves i and vi correspond to bulk polycrystalline Pt and **GC6**, respectively. Both **GC6** and conventional GC20 (Tokai) are essentially inert toward the hydrogen evolution reaction (HER). Curve v was obtained with **PtO_2/GC6** containing 0.25 Pt atom % in the form of microcrystalline PtO_2. Modest electrocatalysis is observed. Curve iv represents 0.90 Pt atom % of nanoscale **Pt-GC6** cured as a solid (ca. 2 × 2 × 10 mm) disk, with current flowing through ~10 mm of the sample. Although substantial catalysis is evident, there is significant ohmic potential error at the fairly large current densities employed. On the basis of the resistivity of **GC6**, the ohmic potential error is at least 50 mV at 25 mA/cm^2. The thin film of **Pt-GC6** (ca. 2 μm thick) on conventional GC greatly reduces ohmic potential error (voltammogram ii), and the 0.90 Pt atom % material is roughly as catalytically active as bulk polycrystalline Pt for equal geometric areas.

A similar comparison for the dioxygen reduction reaction (ORR) is shown in Figure 11. The background corrected curve (ii) for **Pt-GC6** was obtained by subtracting voltammograms recorded after argon degassing and after

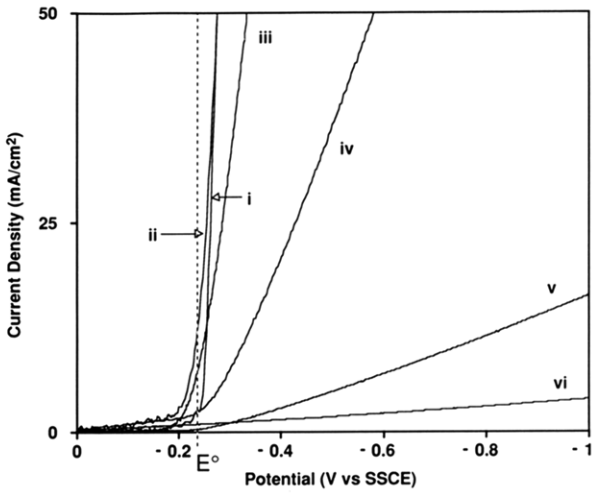

Figure 10. Hydrogen evolution voltammograms obtained in 1 M $HClO_4$, 50 mV/s scan rate. Current density is based on geometric area. Electrode materials were as follows: (i) polycrystalline Pt wire mounted in glass; (ii) 0.90 Pt atom % **Pt-GC6** thin film on commercial (Atomergic GC25) glassy carbon disk; (iii) 0.50 Pt atom % **Pt/F-GC6** thin film on commercial (Atomergic GC25) glassy carbon disk; (iv) bulk sample of **Pt-GC6** containing 0.90 Pt atom %; (v) bulk sample of **PtO_2/GC6** containing 0.50 Pt atom % as PtO_2; (vi) **GC6**.

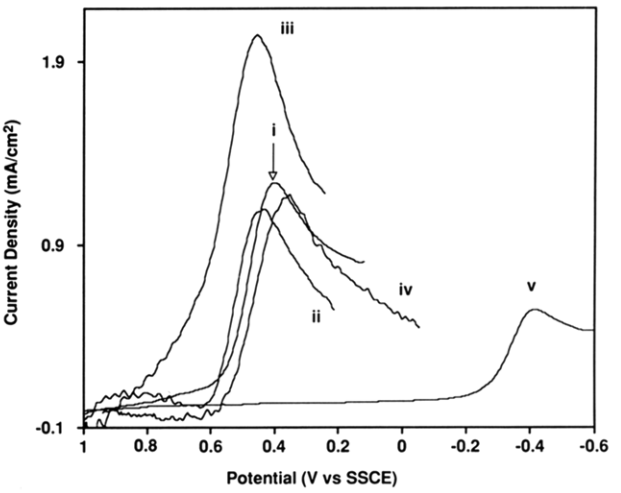

Figure 11. Dioxygen reduction voltammograms obtained in O_2 saturated 1 M $HClO_4$, 50 mV/s. Except for curve iii, voltammograms were corrected by subtracting a voltammogram of an argon purged solution. Electrode materials were: (i) polycrystalline Pt; (iii) 0.90 Pt atom % **Pt-GC6**; (ii) same as iii, but background corrected; (iv) 0.50 Pt atom % **Pt/F-GC6**; (v) **GC6**.

dioxygen saturation. Although **Pt-GC6** exhibits a substantial background current (curve iii), the catalysis of the ORR is comparable to bulk Pt (curve i) of similar geometric area. Assuming a 2-μm-thick film, a film density of 2.2 g/cm^3, and 0.90 Pt atom % in **Pt-GC6**, the Pt loading of the electrodes used in Figures 10 and 11 is 56 μg/cm^2 of geometric electrode area.

Pt/F-GC6 films were also examined to test the hypothesis that a more hydrophobic surface would improve dioxygen reduction kinetics.[33] A GC electrode coated with a thin film of **Pt/F-GC6** (0.5 Pt atom %) yielded voltammogram iii in Figure 10 and iv in Figure 11. These films showed slightly less electrocatalytic activity for the HER and ORR compared to either polycrystalline Pt or **Pt-GC6**. The lower activity may be caused by the low Pt loading compared to the **Pt-GC6** films (19 μg/cm^2 vs ≥56 μg/cm^2 of Pt), but the voltammetry does indicate that the

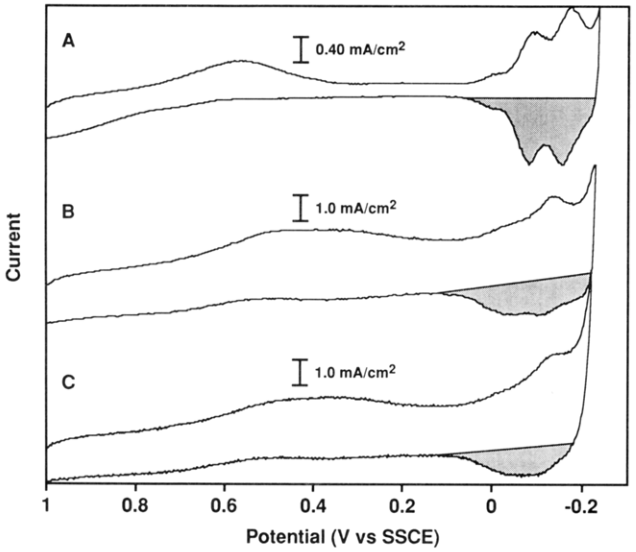

Figure 12. Voltammograms (200 mV/s) obtained in 1 M $HClO_4$, for (A) polycrystalline Pt; (B) 1.1 Pt atom % **Pt-GC6**; (C) 0.90 Pt atom % **Pt-GC6**. The shaded area indicates charge considered to be due to the desorption of adsorbed H atoms.

introduction of fluorine into the GC lattice leads to no dramatic effects on electrocatalysis. However, the relatively hydrophobic surface of the fluorinated films[33] may reduce impurity adsorption and extend the lifetime of the electrode.

The synthetic procedure **Pt-GC6** differs fundamentally from previous procedures involving graphite-supported Pt,[44] electrodeposited Pt on GC,[10,19,25-28] vapor deposition,[56] or formation from impregnated Nafion.[57] Compared to these alternatives, the **GC6** route yields a narrow size distribution of particles, presumably due to rapid cross-linking of the **GC6** host, thus reducing particle agglomeration. The electroformed catalysts often have higher H adsorption areas than **Pt-GC6**, probably because of greater accessibility to the solution. If this is the case, the H adsorption area may be increased for **Pt-GC6** by preparing thinner or more porous films. Since the **Pt-GC6** precursor can be applied as a solution, its concentration on the support surface may be made arbitrarily low.

While comparisons of catalytic activity based on geometric area may be of practical value, it is also useful to consider microscopic area and individual particle activity. The active Pt area was determined from hydrogen desorption measured in 1 M $HClO_4$. Although the active Pt area in **Pt-GC6** will depend on solution accessibility, surface cleanliness, and perhaps particle size, observed H adsorption will at least provide an estimate of accessible microscopic area. Figure 12 shows voltammograms of polycrystalline Pt, 0.90 and 1.1 Pt atom % **Pt-GC6**.

The shaded area of voltammogram A in Figure 12 equals 504 $\mu C/cm^2$ of geometric area for polycrystalline Pt. On the basis of the classical value of 210 $\mu C/cm^2$ for H adsorption, the electrode used here has a roughness factor of 2.4. Voltammogram B in Figure 12, obtained with 1.1 Pt atom % **Pt-GC6**, shows some distortion of the hydrogen adsorption and desorption peaks, but integration of the shaded area yields 150 $\mu C/cm^2$ of geometric area. Thus, a loading level of 66 $\mu g/cm^2$ (based on a density of 2.2 g/cm^3 and a film thickness of 2 μm) of Pt in **Pt-GC6** yields a larger H adsorption area than polycrystalline Pt. For the 0.90 Pt atom % **Pt-GC6**, H adsorption is 987 $\mu C/cm^2$ for a loading of 56 $\mu g/cm^2$ (Figure 12C).

On the basis of the assumption that 8–10-Å Pt particles retain the 210 $\mu C/cm^2$ adsorption of bulk Pt, one can calculate microscopic Pt particle areas of 8.4 and 7.6 m^2/g for the 8- and 10-Å particles, respectively. However, it is unlikely that 8–10-Å particles will exhibit the 210 $\mu C/cm^2$ adsorption observed for bulk polycrystalline Pt, and a more reliable calculation is the ratio of the number of H atoms adsorbed to the total number of Pt atoms present. For the 8 Å **Pt-GC6** film, 6×10^{15} H atoms/cm^2 adsorb on 1.7×10^{17} Pt atoms, assuming a film thickness of 2 μm and film density of 2.2 g/cm^3. Thus, approximately 3.5% of the total Pt atoms are available for H adsorption based on a mechanism involving one H atom per Pt. For the 10-Å **Pt-GC6** film, about 3.2% of the total Pt atoms exhibit H adsorption.

While these results are approximate due to uncertainties about adsorbed impurities, film thickness, film density, and possibly H adsorption mechanism, several observations are available. First, a majority of the total Pt atoms are on the surface of 8–10-Å particles. For example, a cubooctahedral 10.2-Å-diameter Pt cluster contains 38 Pt atoms, of which 24 are on the surface.[54] Second, the high surface/volume ratio leads to H adsorption areas higher than polycrystalline Pt, even though the **Pt-GC6** films are only 0.9–1.1 Pt atom %. Third, the estimated 8 m^2/g active area of the ca 3% active Pt atoms is lower than graphite-supported Pt preparations ($\geq$50 m^2/g) for several possible reasons. Many or most of the Pt particles may be inaccessible to the electrolyte in the **Pt-GC6** films. The Pt surface may be obstructed by adsorbed impurities, or the particles may not have the same hydrogen adsorption capacity as bulk Pt. While these issues remain to be resolved, there is significant headroom for improving catalyst activity by modifying film porosity, thickness, and impurity adsorption.

An additional observation about the H adsorption peaks is more qualitative and relates to distortion of the peaks themselves. Shifts in peak potential have been attributed to changes in the binding energy of adsorbed hydrogen, caused by some change in the electronic nature of the Pt surface.[56] A simple explanation is impurity adsorption, but the distortion may also imply a difference in adsorption behavior between ca. 8-Å particles and bulk platinum. Given that an 8-Å particle has a diameter equivalent to about 3 Pt atoms, the surface will deviate significantly from polycrystalline Pt, and differences in H adsorption behavior would not be surprising. For vapor-deposited platinum particles, Takasu et al. have suggested that the exchange current density for the HER was greater with smaller particles because of a greater ratio of edge/terrace sites and that the hydrogen adsorption strength was weaker with decreasing particle size.[56]

The results presented thus far establish that **Pt-GC6** provides efficient use of precious metal catalyst, mainly through a high surface/volume ratio. This is an obvious advantage with respect to potentially reducing catalyst cost in electrocatalytic applications. The results also address a fundamental question about reactivity differences between small particles and bulk platinum. The experiments described below bear on a single question: do nanoscale Pt particles in **Pt-GC6** behave qualitatively

(56) Takasu, Y.; Fujii, Y.; Yasuda, K.; Iwanaga, Y.; Matsuda, Y. *Electrochem. Acta* **1989**, *34*, 453.
(57) Liu, R.; Her, W.-H.; Fedkiw, P. S. *J. Electrochem. Soc.* **1992**, *139*, 15.

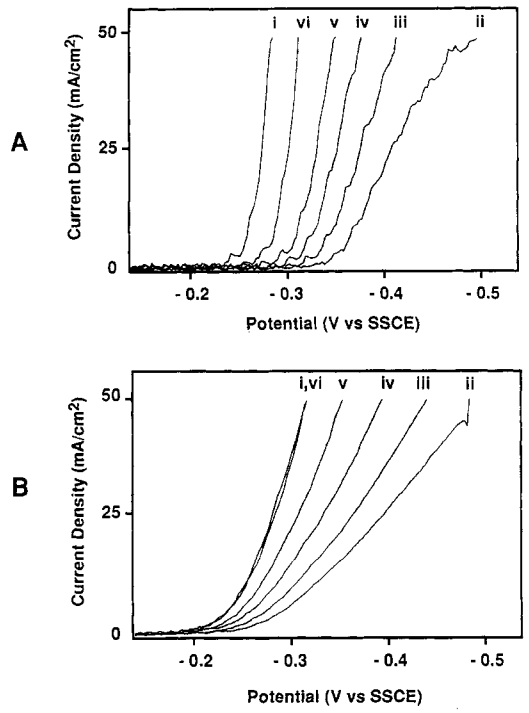

Figure 13. Voltammograms (50 mV/s) from $HClO_4/NaClO_4$ solutions obtained on (A) polycrystalline Pt, and (B) 0.90 Pt atom % **Pt-GC6** thin film electrode. Voltammograms were obtained in the numerical order indicated, and the ionic strength was kept constant throughout. $HClO_4$ concentrations were (i) 1.0, (ii) 0.0625, (iii) 0.125, (iv) 0.25, (v) 0.5, (vi) 1.0 M.

identically to bulk Pt toward H^+ reduction, or is there some change in mechanism when the particle size approaches atomic dimensions? It is not our intent to fully investigate the HER mechanism on nanoscale Pt particles, which is probably at least as complex as that on bulk platinum. Rather, we intend to establish any qualitative differences in the hydrogen evolution reaction between ca. 8-Å platinum particles in **Pt-GC6** and polycrystalline platinum.

Figure 13 shows voltammograms for the HER on bulk Pt and 8-Å **Pt-GC6** for several acid concentrations. Curves i and vi were both for 1 M $HClO_4$, but at the beginning (i) and end (vi) of the series. Although polycrystalline Pt exhibits the expected shifts in overpotential with H^+ activity, there is some deactivation of the surface during the series of voltammograms. **Pt-GC6** also shows the potential shift, but the electrode performance is more stable.

The data of Figure 13 may be considered more quantitatively by examining several kinetic parameters, summarized in Table I. The Tafel slope refers to the plots of ln (i) vs overpotential (η) for HER in 1 M $HClO_4$. Slopes were determined in the low overpotential region 10–40 mV and the exchange current density was determined by extrapolating to zero potential. The reaction order for H^+ was determined from the steady-state H^+ reduction current at $\eta = 50$ mV, in solutions of constant ionic strength but H^+ concentrations from 1.0 to 0.06 M. The slopes of log i vs log $[H^+]$ yield the reaction order in H^+. It is well recognized that a variety of phenomena can affect these kinetic observables, some of which are not well controlled (e.g., surface cleanliness, mass transport in GC film, etc.). However, comparison of such parameters for bulk Pt and **Pt-GC6** can provide some insight into the nature of the HER at small Pt clusters.

Table I. Hydrogen Evolution Kinetic Parameters for Polycrystalline Platinum and Pt-GC6 Materials

electrode	Tafel slope[a] (V^{-1})	d(log i)/ d(log C_{H^+})[b]	exchange current density[c] (mA/cm^2)	exchange current density[d] (mA/cm^2)
polycrystalline Pt	33	1.9 ± 0.1	1.0	0.42
⟨8 Å⟩ Pt-GC6	11	1.1 ± 0.1	9.3	2.0
⟨10 Å⟩ Pt-GC6	20	1.2 ● 0.2	3.3	0.67
⟨15 Å⟩ Pt-GC6	23	1.5 ± 0.2	1.8	0.30

[a] From plot of log i vs E for range of η = 10–40 mV. 33 V^{-1} is equivalent to the often used notation of $(30\ mV)^{-1}$. [b] Determined at $\eta = 50$ mV. [c] Based on geometric area. [d] Based on H adsorption area, assuming 210 $\mu C/cm^2$.

The kinetic parameters for polycrystalline Pt are typical, exhibiting second order in H^+ and a Tafel slope of 33 V^{-1}.[58] Although other interpretations are possible, the usual mechanism proposed for this case is a rate limiting combination of adsorbed H atoms at low overpotential. The data of Table I indicate that the **Pt-GC6** materials behave quite differently. First, the order of H^+ is close to 1 for the 8-Å **Pt-GC6** surface, implying a different rate limiting step. Second, the smaller Tafel slope implies a smaller value of α for the **Pt-GC6** case. Given the well-known complexity of the HER on well-defined Pt surfaces, it would be risky to draw extensive mechanistic conclusions from these results. However, it is clear that the mechanism or rate-determining step, or both, on **Pt-GC6** differs from that on polycrystalline Pt. Thus the Pt particles in **Pt-GC6** are not behaving merely as small versions of polycrystalline Pt but rather exhibit qualitative as well as quantitative differences in HER behavior.

The distinct behavior of **Pt-GC6** could be attributed to the carbon matrix, e.g., adsorbed impurities from the organic precursor, mass-transfer effects, etc. Alternatively, it could be caused by changes in mechanism with particle size. Smaller particles have a high ratio of vertices and edges to crystallite faces, so that a ca. 10-Å particle is nearly "all edge". Perhaps the HER mechanism is quite different for a case where the edge or vertex sites dominate. Some evidence to distinguish between carbon matrix effects and particle size effects is provided by Table I. For the three **Pt-GC6** materials, one would expect the carbon matrix to be similar. As the particle size and Pt loading increase, however, the H^+ order and Tafel slopes approach those of polycrystalline Pt. This observation is strong evidence that the kinetic differences between **Pt-GC6** and polycrystalline Pt are due to particle size effects rather than the GC matrix.

Particle size effects on the hydrogen and oxygen reactions have been considered previously in terms of the edge/terrace ratio. Takasu et al. reported that the specific activity (exchange current per unit of H adsorption area) continued to increase as particle size decreased, consistent with the behavior of **Pt-GC6**.[56] Figure 14 illustrates the specific activity for the HER on **Pt-GC6** as a function of particle size. Takasu's observations (open circles), as well as the fraction of vertex sites are also shown. The **Pt-GC6** materials show the same trend in current density as vapor-deposited particles but with smaller particle diameters. Furthermore, the increase in current density tracks the number of vertex sites, implying a dependence of HER

(58) Greef, R.; Peat, R.; Peter, L. M.; Pletcher, D.; Robinson, J. *Instrumental Methods in Electrochemistry*; Ellis Horwood: London, 1985; p 233.

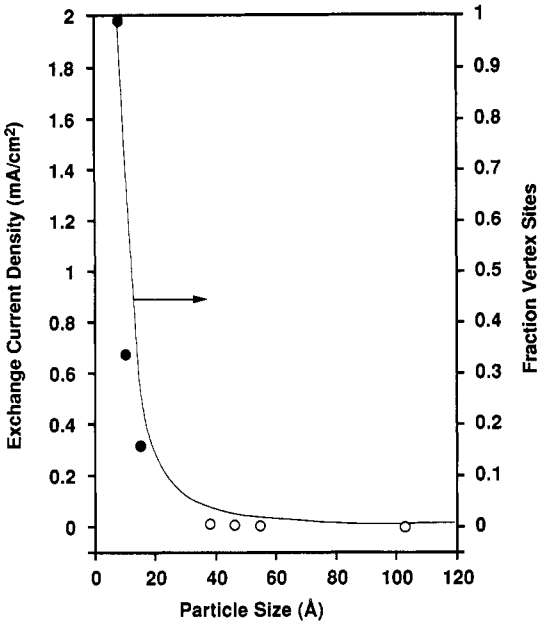

Figure 14. Exchange current density, based on H adsorption area, for **Pt-GC6** (closed circles) as a function of mean particle size. Open circles are for vapor-deposited Pt.[56] The solid line and right-hand ordinate show the fraction of vertex sites (relative to total Pt atoms) for cubooctahedra with indicated particle diameters.

catalysis on Pt sites which predominate for smaller particles. For O_2 reduction, Kinoshita noted a decrease in activity below about 35-Å particle diameter, which he attributed to the importance of terrace sites.[44] The current results do not permit verification of this observation for oxygen reduction. An additional consequence of particle size was reported by Christensen et al., who concluded that CO does not adsorb to small Pt particles and is not the poison which reduces catalytic activity.[59] If such an effect occurs on **Pt-GC6**, it may be of significant practical value.

Conclusion

The fundamental novelty of our approach is the synthesis of new carbon matrices which, by necessity, result in the formation of new carbon-based surfaces rather than the superficial chemical modification of conventional glassy carbon. The incorporation of platinum in the GC precursor results in the formation of nanoscale, crystalline platinum(0) clusters with controlled dimensions. The electrocatalytic response of these materials is a function of the size of the platinum clusters contained in the solid. In addition, the activity of the platinum doped glassy carbons for both the hydrogen evolution and oxygen reduction reactions is extremely high with excellent stability.

Acknowledgment. We are grateful to the National Science Foundation (CHE-9007132) for their financial support of this work. We also thank Fort Fibres Optiques (Paris) for a scholarship to N.L.P. and the Center for Materials Research of the Ohio State University for partial support of this effort. We thank Dr. Hendrik Colijn and Ms. Claire MacDonald of the Central Electron Optics Facility (OSU) for their assistance with the TEM and SEM analyses, Mr. Roy Tucker (OSU) for his assistance with the XPS analyses, and Mr. Carl Engleman (OSU) for his assistance with the NMR analyses.

(59) Christensen, P. A.; Hamnett, A.; Weeks, S. A. *J. Electroanal. Chem.* **1988**, *250*, 127.